Experimental Investigation of Aerodynamic Interactions of a Wing with Deployed Fowler Flap under Influence of a Propeller Slipstream

Duivenvoorden, R.R.; Suard, Noah; Sinnige, T.; Veldhuis, L.L.M.

DOI
10.2514/6.2022-3216

Publication date
2022

Document Version
Final published version

Published in
AIAA AVIATION 2022 Forum

AIAA AVIATION Forum
June 27-July 1, 2022, Chicago, IL & Virtual
AIAA AVIATION 2022 Forum

10.2514/6.2022-3216

Experimental Investigation of Aerodynamic Interactions of a Wing with Deployed Fowler Flap under Influence of a Propeller Slipstream

R.R. Duivenvoorden*
Delft University of Technology, Delft, The Netherlands
Institut für Flugantriebe und Strömungmaschinen, TU Braunschweig, Germany
Cluster of Excellence "Sustainable and Energy-Efficient Aviation - SE^{2}A", EXC2163/a, TU Braunschweig, Germany

N. Suard†, T. Sinnige‡ and L.L.M. Veldhuis§
Delft University of Technology, Delft, The Netherlands

Experiments were performed using a wall-to-wall unswept and untapered wing with a single slotted flap and a propeller, to obtain a validation dataset and gain insight into primary flow phenomena in propeller-wing-flap interactions. Measurements were taken using pressure taps, a wake rake and oil flow visualization, for several flap deflections (0, 15 and 30 degrees) and thrust settings (unpowered, $J = 0.8$ / $T_c = 1.05$ and $J = 1.0$ / $T_c = 0.45$). Similarity of the measured data to similar experiments was poor, which was believed to be due to the low Reynolds number of $Re = 6e5$ and sensitivity of local measurements due to occurrence of stall cells. Oil flow visualizations showed significant induction of flow separation from nacelle-wing interactions in unpowered conditions, traced to boundary layer growth. For powered cases it was shown that both sides of the deployed flap are immersed in the part of the slipstream that passes the pressure side of the main element. This part of the slipstream deforms significantly before it reaches the flap and thus results in complex spanwise variations for the flap flow. This stresses the need to investigate slipstream development in propeller-wing-flap systems and the effects on flap flow specifically to gain in-depth understanding of the interactions. The results presented in this paper expose the inherent complexity of investigating propeller-wing-flap systems and gaining viable validation data, and might serve to guide for future investigations of propeller-wing-flap systems.

I. Introduction

In recent years, the application of propellers to augment high-lift performance of aircraft has regained favor in next-generation aircraft concepts due to the possible synergies with distributed electrical propulsion and the renewed attention for propeller for the sake of propulsive efficiency. Significant work on propeller-blown high-lift augmentation has been published in the 1950s, e.g. by Kuhn and Draper [1–3], focused on achieving fixed-wing VTOL capability. Ultimately, these efforts were unsuccessful, as the required slipstream turning angles for VTOL capable fixed-wing aircraft required mechanically complex systems of flaps and vanes and were coupled with undesirable moment coefficients.

More contemporary research on the topic focuses on relatively simpler combinations of (tractor) propeller-wing-flap (PWF), often combined with distributed propulsion, in order to satisfy high-lift requirements for landing with slender wing planforms optimized for cruise conditions. A popular example is the LEAPTech aircraft [4–6] and its successor, the X-57 Maxwell. Out of modern literature on PWF systems, most focus on impact on wing performance metrics [7–9], but often do not characterize the phenomena that these metrics are dominated by. Others focus on reduced-order modeling

*PhD Candidate, Delft University of Technology, faculty of Aerospace Engineering, department of Flight Physics and Technology, Kluyverweg 1, 2629HS, Delft, The Netherlands, AIAA member.
†MSc Student, Delft University of Technology, faculty of Aerospace Engineering, department of Flight Physics and Technology, Kluyverweg 1, 2629HS, Delft, The Netherlands.
‡Assistant Professor, Delft University of Technology, faculty of Aerospace Engineering, department of Flight Physics and Technology, Kluyverweg 1, 2629HS, Delft, The Netherlands, AIAA member.
§Professor, Delft University of Technology, faculty of Aerospace Engineering, department of Flight Physics and Technology, Kluyverweg 1, 2629HS, Delft, The Netherlands, AIAA member.

capabilities [10] or consider non-standard flap configurations that make it difficult to relate to slotted multi-element wings [11].

Fundamental descriptions of the aerodynamic interactions that dominate the PWF system and, in particular, how these differ from related sub-fields like propeller-wing interaction and multi-element aerodynamics, are still lacking in literature for PWF systems. Notable literature on propeller-wing interaction [12–14] focus mostly on cruise conditions and single-element wings, and while some literature on propeller slipstream development in the presence of a wing does include the high-lift condition [15, 16], there is little attention for the interaction with the flap as a separate element in the system.

The present paper describes the results of an early experiment in a project to improve aerodynamic understanding of the interactions that dominate the flowfields of propeller-wing-flap systems, performed in May 2021. It confirms knowledge available from literature and notes several aspects of the aerodynamic interactions specific to the presence of a flap that are believed to be underappreciated in the currently available literature.

II. Experimental Setup

Experiments were performed in the Low Turbulence Tunnel (LTT) at the Delft University of Technology, a closed single-return tunnel with a turbulence level of approximately 0.015% at the testing velocity of 30 m/s. The tunnel features interchangeable test sections with an octagonal cross section. These test sections have a width of 1.8m, a height of 1.25m and length of 2.6m.

A. Model Geometry

The unswept, untapered wing model featured a NLF-Mod22(B) airfoil, originally designed by Boermans and Rutten [17], with a chord-length of 0.3 m and span of 1.248 m (clamped to the tunnel using shims). The airfoil is shown in Fig. 1. A single-slotted flap of 30% chord could be positioned in one of three configurations, namely flap nested, flap deployed at 15 degrees with 8% overlap and 2% gap, and flap deployed at 30 degrees with 0% overlap and 3% gap. Definitions of deflection (δ_f), overlap (dx) and gap (ds) are given in figure 2. The flap was attached to the the main element with a set of 6 brackets, as shown in Fig. 3. The main element of the wing was mounted vertically in the test section, clamped to the wind tunnel walls on both sides. The gap between the flap and the wind tunnel wall was taped off in order to avoid bleed flow. A technical drawing of the wing model with relevant dimensions and definition of axes is provided in Fig. 4.

The model was purposely built to hold up to three nacelles and propellers, though for the purposes of the present experiment only a single one was used, mounted on the wing centerline. The nacelle housing was a relatively long and thin cylinder, angled 5 degrees downwards with respect to the wing chord, putting the propeller at roughly 0.85D from the wing leading edge. The propeller was a TUD-XPROP-S reference propeller, with a diameter of 203.2 mm and a blade pitch of $\beta_{0.7R} = 30$ degrees. Due to limitations of the electric motor, the propeller was limited to an advance ratio of $J = 0.8$ at a windtunnel velocity of 30 m/s, which would correspond to a thrust coefficient of $T_c = 1.05$ in isolated propeller conditions.

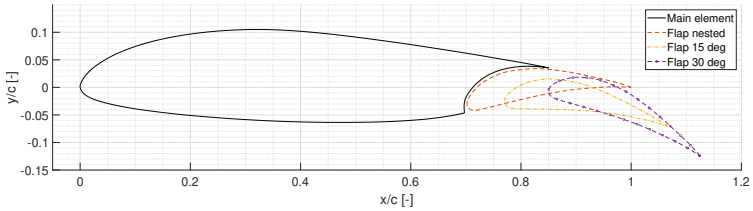

Fig. 1 NLFmod22(B) profile with flap nested, flap deployed at 15 degrees ($dx = 8\%$, $ds = 2\%$) and flap deployed at 30 degrees ($dx = 0\%$, $ds = 3\%$).

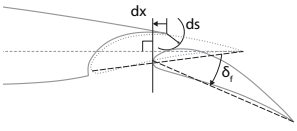

Fig. 2 Definition of δ_f, ds and dx.

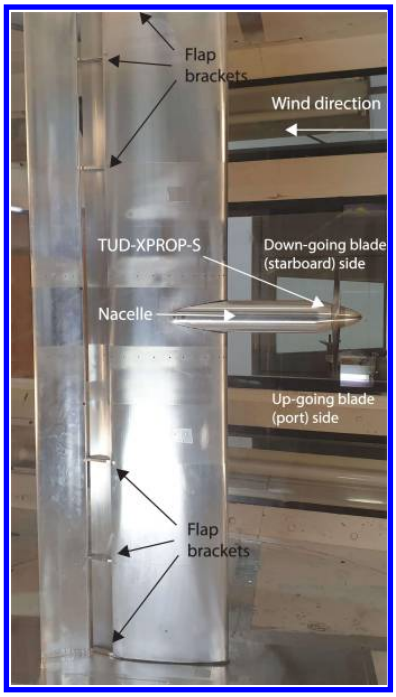

(a) Pressure side

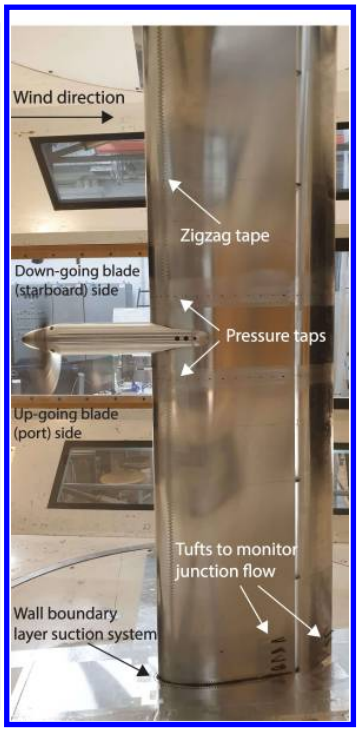

(b) Suction side

Fig. 3 Wing as placed in the test setup with flap deployed and nacelle and prop attached.

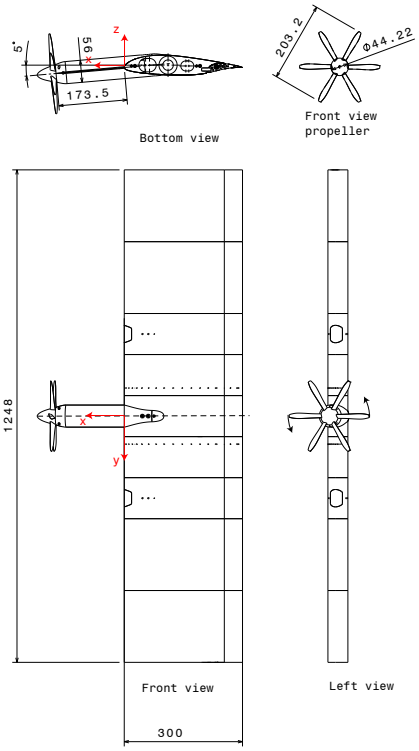

Fig. 4 Technical drawing of wing model. Dimensions in mm.

B. Wall boundary layer suction

In previous (as of yet unpublished) experiments with the same model in a different wind tunnel, strong junction flows were observed at the wing-wall boundary that induced early onset of separation. In order to mitigate these effects, a wall boundary layer suction (BLS) system was applied, based on the system applied in the original reports of the NLF-Mod22(B) profile by Boermans and Rutten [17]. Figure 5 shows the row of holes in the wall end plate, present at both sides of the model, which were externally connected to a suction pump. Because the flap was to be moved throughout the experiment, suction holes were only applied around the main element. The interaction between the wing and the wall boundary layer of the wind tunnel in the presently described experiments was found to lead to no appreciable affect of the BLS on any of the measurements taken. The results presented in this paper are therefore all captured without application of BLS.

Fig. 5 Holes in the side plate around the main element of the wing for the suction system.

C. Measurement Techniques

The model includes two chordwise rows of pressure taps at $y/b = \pm 0.35D$, on each side of the wing centerline. Measurements of all taps were taken simultaneously using an electronic pressure scanner with a sampling frequency of $10\,Hz$ and a measurement time of 10 seconds per angle of attack. Figure 6 shows the chordwise distribution of the pressure taps over the airfoil, which are tabulated for reference in Tables 2 and 3 in Appendix IV.A.

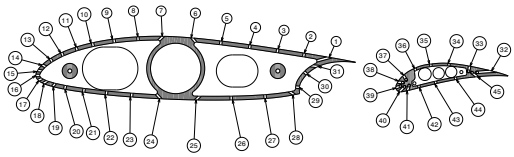

Fig. 6 Chordwise distribution of pressure taps on main element and flap.

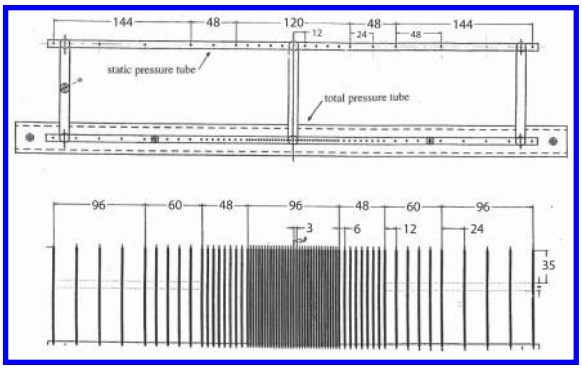

Fig. 7 Wake rake top and front view with spacing dimensions indicated in mm. Modified from [17]

A wake rake with total and static pressure probes was placed at a downstream location of $x/c = 2$, meaning the tips of the probes were positioned one chord-length from the wing trailing edge with flap nested. Figure 7 shows the dimensions and spacing of the probes. The wake rake was traversable in both spanwise and normal directions. Resolution of measurement points was 10 mm in spanwise direction, while in normal direction the wake rake was aligned with the center of the wing wake, with additional measurements at ±99 mm from the wake center. This ensured a resolution of 3 mm within ±40mm from the test section centerline due to the distribution of probes on the wake rake. The wake rake and support rig was only fitted in the tunnel during the slipstream/wake measurements and removed for all other measurements, including polar measurements using the pressure taps on the wing, in order to avoid interference effects. This means that no profile drag estimations based on wake deficiencies were performed and only pressure drag data was available. Measurements were taken by the same electronic pressure scanner as the pressure taps were attached to, but at a measurement time of 5 seconds.

Finally, oil flow visualization was performed for most configurations at various angles of attack. The flow visualization oil was a mixture of light paraffin oil with UV-luminescent material. The images were taken with a DSLR camera while the wind tunnel was running. It should be noted that as the wing was mounted vertically in the wind tunnel, gravity plays a significant role in the transport of the oil, particularly in areas where the shear forces are low. The oil flow thus indicates dominant flow direction in regions of high shear, but cannot be completely interpreted as streamlines of the flow.

D. Configurations

Table 1 shows an overview of the configurations considered in the experiment. Due to time constraints, configuration 5 was limited to wake rake measurements only at $J = 0.8$ and is not discussed further in this paper. All other powered cases were run at $J = 0.8$ and $J = 1.0$, corresponding to a high thrust coefficient ($T_c = 1.05$) and maximum propeller efficiency ($T_c = 0.45$). The former was the maximum thrust coefficient achievable for an isolated propeller considering the electric motor used and the selected freestream velocity.

Table 1 Overview of tested configurations.

CF	δ_f [^{o}]	ds [$1/c$]	dx [$1/c$]	Nacelle	Prop
1	0	-	-	Off	Off
2	15	0.02	0.08	Off	Off
3	30	0.03	0	Off	Off
4	30	0.03	0	On	Off
5	30	0.03	0	On	On ($\beta_{0.7R} = 45°$)
6	30	0.03	0	On	On ($\beta_{0.7R} = 30°$)
7	15	0.02	0.08	On	On ($\beta_{0.7R} = 30°$)
8	15	0.02	0.08	On	Off
9	0	-	-	On	Off
10	0	-	-	On	On ($\beta_{0.7R} = 30°$)

III. Results and Discussion

The results of the experiment are discussed in this chapter and compared with available literature. The clean wing configuration is presented as a baseline and compared with reference data of the same profile in order to contextualise the interpretation of the available data. Subsequently, nacelle-wing interaction, propeller-wing interaction as well as propeller-wing-flap interactions are evaluated. All coefficients resulting from pressure tap measurements are denoted with an asterisk, to indicate the fact that they are local sectional measurements and should not be considered to necessarily represent flow characteristics at other spanwise stations. This is treated in more detail in section III.A.3.

A. Baseline Measurements

Figure 8 shows the aerodynamic coefficients obtained from the pressure tap measurements during the experiment, in comparison with data obtained by Boermans and Rutten [17] in reference experiments using the same airfoil. It should be noted that the 30 degrees flap case by Boermans features 0.5% overlap rather than 0% as in the present experiments. Both the present (LTT) and data from Boermans and Rutten (Boermans) have been corrected for windtunnel boundary effects using the method by Allen and Vincenti [18], however, for the present experiments the wake blockage correction is only based on pressure drag. Whereas Boermans and Rutten report total drag extracted from wake rake measurements, no such data was available for the LTT experiments. The wake blockage correction for the LTT data is therefore slightly undervalued, though this is expected to be within 1% of the respective coefficient values as the model chord of 0.3m is small compared to the wind tunnel width of 1.8 m (since the model is mounted vertically).

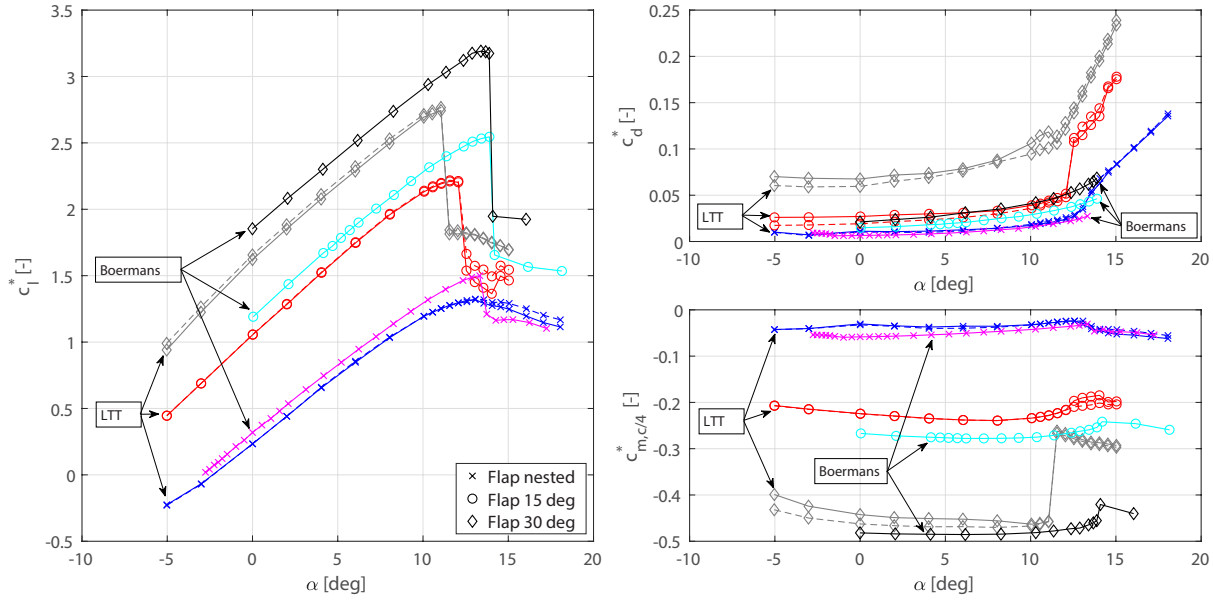

Fig. 8 Integrated local pressure measurements versus angle of attack for clean wing configurations in the LTT experiment versus reference [17]. Solid and dashed lines of LTT data represent respectively starboard- and port-side pressure tap locations.

The results obtained by Boermans and Rutten [17] are different from the results obtained in the presently described experiment, as can be seen from Fig. 8. The lift coefficient with flap nested is consistently higher in the Boermans data than in the present experiment and it shows leading edge stall characteristics, while the present experiment shows signs of more gradual trailing edge stall. The discrepancy between Boermans and LTT data increases when a flap is deployed, showing significantly higher flap effectiveness in the Boermans experiments, with more lift generated across the polar and a higher angle of maximum lift. The moment coefficients fall closer together for both experiments, with the major discrepancy found in the 30 degrees flap case, which shows a large jump post-stall due to complete flow separation on the flap. The Boermans data shows flow on the flap to remain attached despite the main element stalling and thus shows a much smaller change in moment coefficient.

There are several phenomena that occurred during the LTT experiments that are likely to cause the observed differences in performance. These phenomena are described in detail below in an attempt to provide a solid context for the interpretation of data in the remainder of the paper.

1. Reynolds and Mach Number Effects

At least a part of the observed differences between the LTT and Boermans results can be attributed to Reynolds number effects. The Boermans experiments were performed at $Re = 3E6$ for the flap nested case, $Re = 2E6$ for the 15 degrees flap and $Re = 1.7E6$ for the 30 degrees flap, while the LTT experiments were all performed at approximately $Re = 6E5$. This meant that laminar separation bubbles could occur, which were observed with the 30 degree flap case. Increases in angle of maximum lift are in line with what would be expected of Reynolds number effects in this critical range [19]. Mach number effects may also play a role, particularly for the flapped cases. Though these effects have not been investigated specifically, they are expected to be small. The LTT experiments were performed at $M = 0.088$ for all configurations, while the Boermans data were captured at $M \approx 0.23$, $M \approx 0.15$ and $M \approx 0.12$ for flap nested, flap 15 degrees and flap 30 degrees cases, respectively.

2. Boundary Layer Transitioning

As one of the objectives of the experiment was to provide validation data for numerical simulations, as well as due to concerns over the low Reynolds numbers, a fixed point of boundary layer transitioning was desirable. Tripping the boundary layer also avoided the formation of a laminar separation bubble on the main element. The experiments by Boermans and Rutten [17] did not include forces transition of the upper surface of the wing. Several boundary layer tripping methods were tested on the wing, including carborundum grit and several variations in terms of thickness and width of zigzag tape, all applied at 10% chord on the upper surface of the wing. It was noticed that the method of boundary layer tripping has a significant effect on the performance of the clean wing, as exemplified in Fig. 9 where integrated pressure measurements for the wing without forced transition, transition using carborundum grit and transition using zigzag tape of 0.255mm high and 12mm wide are compared. Both tripping methods show a reduction in maximum lift coefficient and a decambering effect on the lift curve slope, particularly the carborundum strip. The local moment coefficient is also reduced significantly for nearly the entire range of angle of attack for both applications of boundary layer tripping when compared to the untripped case.

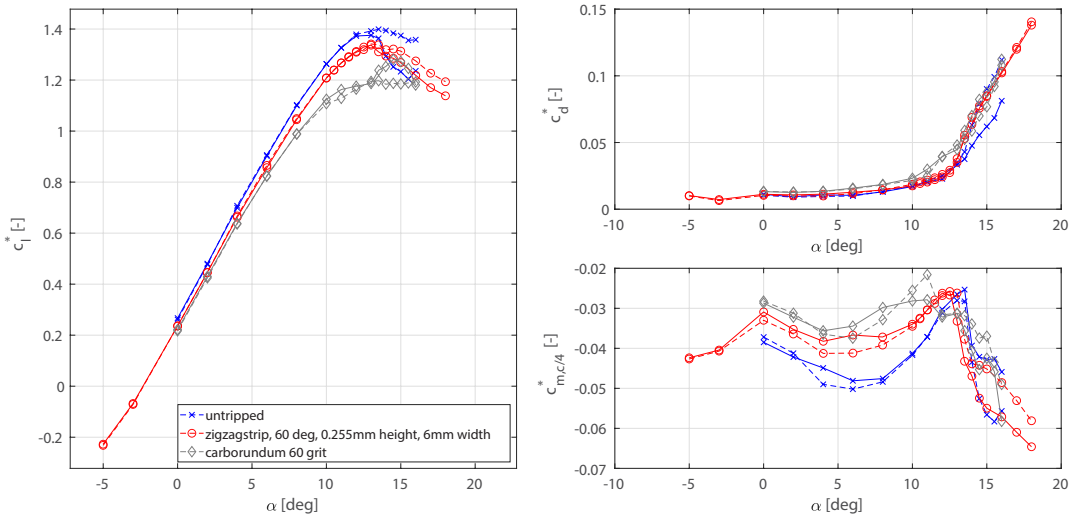

Fig. 9 Integrated local pressure measurements versus angle of attack for various methods of boundary layer tripping, showing significant decambering compared to the untripped lift polar.

Application of distributed roughness through carborundum grit is a tried and tested method [19] and the required grit size had been calculated using the method by Braslow [20]. It was, however, applied to the wing using a thin

double-sided adhesive, which may have caused the effective roughness size to be unintentionally large (though it should be noted that the combined thickness is still less than the better performing zigzag tape). Another explanation might be excessive application of grit, as suggested by Barlow et al. [19]. In the end, the experiment was performed using the zigzag tape of 0.255mm height and 12mm width, as it showed the best performance compared to the untripped wing, while still providing a forced point of transition. Due to the width of this zigzag tape, it was not feasible to apply it to the flap, which was therefore left to transition naturally. Forcing the boundary layer transition also mitigated some of the significant spanwise flow asymmetry that occurred on the wing, as can be observed particularly in the post-stall regime of the untripped polar in Fig. 9 where the starboard and port-side measurements diverge. This phenomenon will be treated next.

3. Spanwise variations

During baseline measurements of the clean wing at high angles of attack, low-frequency unsteady behavior of pressure measurements was noticed along with the existence of spanwise variation of flow separation on the wing. The latter are visualized using tufts in Fig. 10. The observations are consistent with observations made on other quasi-2D windtunnel setups, such as by Winkelmann and Barlow [19], Yon and Katz [21] and more recently Broeren and Bragg [22]. Broeren and Bragg [22] specifically describe the existence of two types of post-stall behaviours, namely stall cells as three dimensional structures and low-frequency unsteady oscillations.

Addition of the zigzag tape improved two-dimensionality of the flow, resulting in less divergence between starboard- and port-side pressure tap measurements, but spanwise variation was not fully eliminated. The model with nacelle mounted no longer showed clear stall cells, but still exhibited spanwise asymmetry at higher angles of attack. This is consistent with observations by Winkelmann and Barlow [23] and Yon and Katz [21], who note a correlation between the wing aspect ratio and the number of stall cells that form. Considering the nacelle to effectively slice the wing into two low aspect ratio parts, this would eliminate the possibility for a full stall cell to develop but would not solve the spanwise asymmetry. For the interpretation of the pressure measurements, this means that they should always be treated as local measurements only and cannot represent the complete wing, even in clean wing configuration. For this reason, all results from the pressure measurements presented in this paper are marked with an asterisk to signify their spanwise dependency.

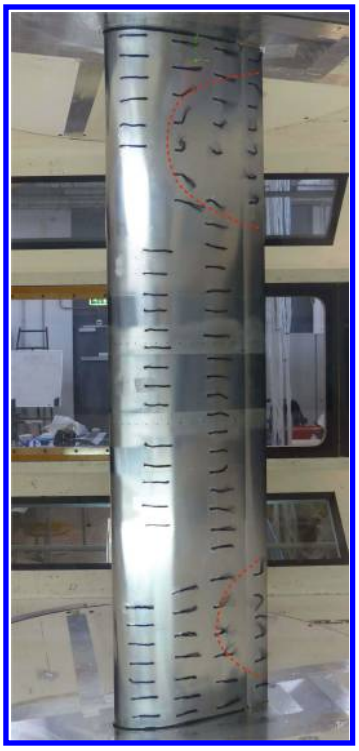

Fig. 10 Stall cells occurring on the clean wing with flap nested at $\alpha = 13^o$ visualized by tufts.

B. Nacelle Interference

The presence of the nacelle to the wing introduces several nacelle-wing interaction effects that will be evaluated and discussed in this section based on oil flow visualisation (OFV) and local pressure data. It should be noted that the structures and phenomena discussed in this section are believed to be qualitatively independent of the occurrence of stall cells and spanwise variations discussed in section III.A.3. This assumption is based on preliminary numerical simulations of the setup, which show the same major structures and phenomena.

1. Local Aerodynamic Coefficients

Figure 11 shows the local aerodynamic coefficients at the two pressure tap locations for the clean wing and nacelle on configurations. For the flap nested cases, negligible effect of the presence of the nacelle to lift, pressure drag and moment is observed. In the post stall regime, the nacelle-mounted case for the nested flap displays some irregular behavior, which is attributed to separated flow instabilities as addressed in section III.A and should be interpreted with caution.

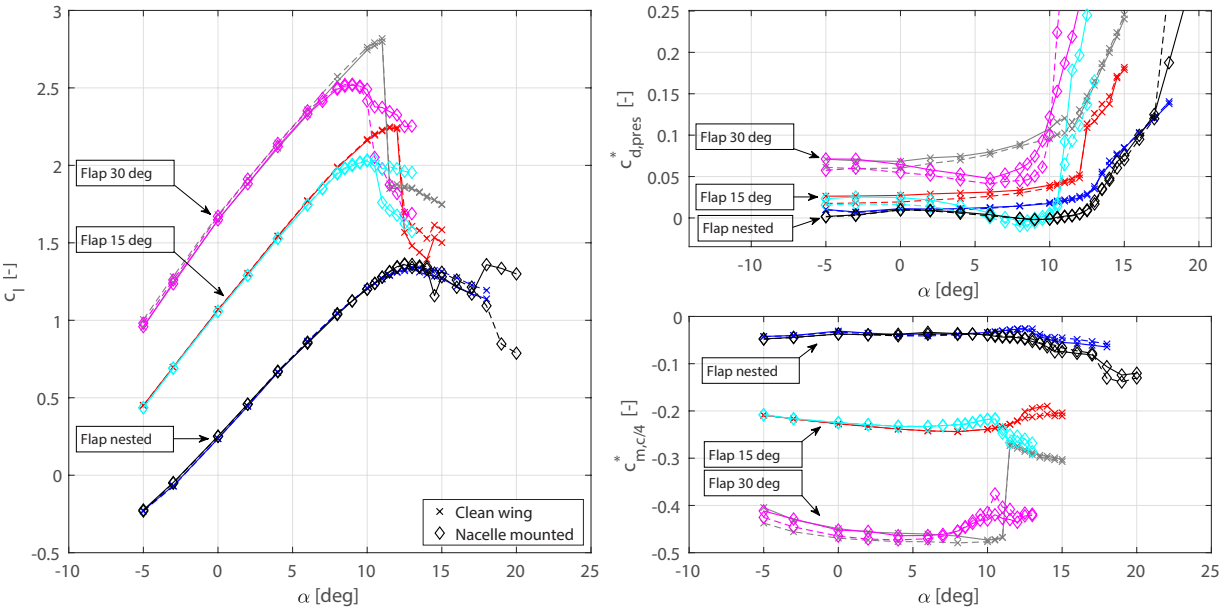

Fig. 11 Integrated local pressure measurements versus angle of attack for the clean wing and nacelle on configurations of each flap deflection. Dashed and solid lines represent respectively starboard- and port-side pressure tap locations. Uncorrected wind tunnel data.

For the flapped cases the addition of the nacelle introduces a large decrease in maximum lift coefficient and angle of maximum lift. Past the angle of maximum lift, the two pressure tap locations also diverge strongly in achieved lift coefficient, which oil flow visualization shows to be related to spanwise asymmetry in flow separation and crossflow at the location of the pressure taps, making analysis based on the integrated coefficients ineffective in these interactive regions of the wing.

In the region of α = 5 to 10 degrees, both flapped cases also show a negative slope in the pressure drag. This is likely related to the suction peak at the leading edge of the main element due to the blockage of the nacelle, as is known to be present from literature [24]. The relative contribution to pressure drag by main element and flap in these cases supports this conclusion, as the main element has negative drag contributions at low angles of attack. The case with 30 degrees flap and nacelle mounted no longer displays the jump in moment coefficient that is observed on the clean wing around α = 11 degrees, which was caused by complete separation of the flap flow. Local pressure distributions show that the separation on both flap and main element are more gradual with the nacelle mounted.

2. Interactive Flow Phenomena

Oil flow visualizations performed during the experiment (Fig. 12) show clear effects of the nacelle on the wing flow, particularly at high angles of attack. A region of spanwise divergent flow is present behind the nacelle (I), which remains attached long after the rest of the wing flow has separated (the thick dashed line indicates the approximate location of the separation line). This is consistent with what is found in literature, such as the study by Qiu et al. [24], where the effective removal of the wing leading edge due to the nacelle placement causes a high pressure region behind the nacelle. The flow in this region expands due to the spanwise pressure gradient and the expansion increases as circulation on the rest of the wing increases, e.g. due to flap deployment or an increased angle of attack.

At higher angles of attack a wedge-shaped separation line (II) can be observed, as flow separation on the wing is expedited at the regions close to the nacelle. Numerical simulations of the experimental setup have confirmed this to be related to boundary layer thickening originating from the nacelle-wing junction (III), primarily fed by the crossflow coming from the high-pressure region. Qualitatively similar results have been reported by Qiu et al. [24], where a combination of an increased pressure peak due to the nacelle blockage along with the spanwise flow due to the high-pressure region caused boundary layer thickening resulting in early onset of separation.

It should be noted that the observed flow separation is not related to vortices shed by the nacelle itself. Radespiel [25] shows nacelle vortices moving over the wing and inducing flow behavior similar to what is observed by Qiu et al. [24] and in the OFV presented in Fig. 12. Numerical simulations of the presently described experimental setup have shown these vortices to occur on the nacelle, but they move over the wing close to the nacelle centerline and are relatively weak as a result of the size and shape of the nacelles. Figure 12b shows some induced separation on the trailing edge of the wing right behind the nacelle (IV), which are believed to be related to these vortices. The position and strength of the nacelle vortices and the boundary layer accumulation at the nacelle-wing junction, as well as whether both effects are likely to combine (as seems to be the case in Radespiel [25]), will depend on the particular nacelle geometry and wing integration and warrants further research.

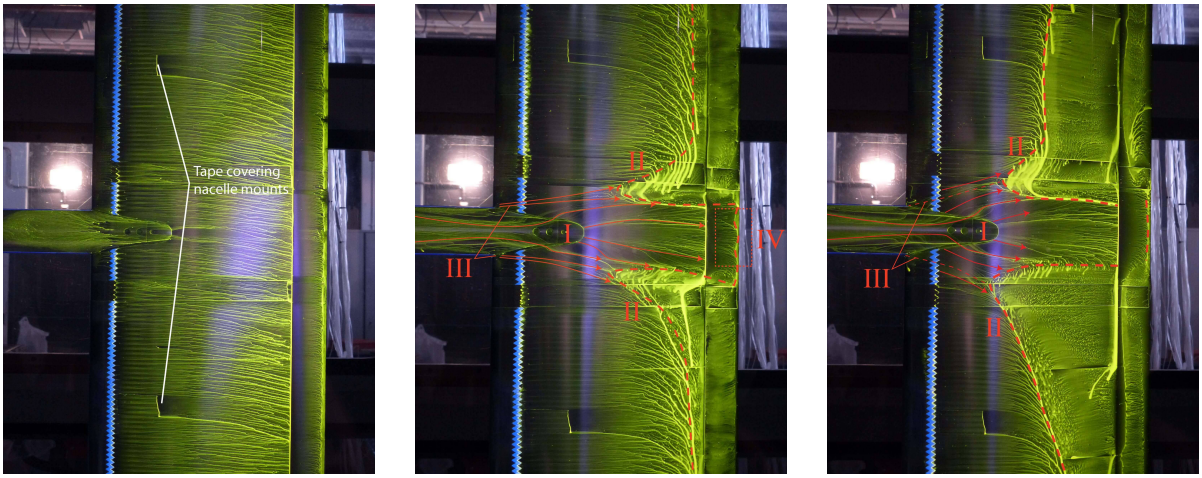

(a) $\alpha = 0°$ **(b)** $\alpha = 10°$ **(c)** $\alpha = 13°$

Fig. 12 Oil flow visualization images of the wing with flap nested and nacelle installed (CF9), showing attached flow directly behind the nacelle and early onset separation originating from the nacelle-wing junction. Dashed line indicates the approximate separation line.

When flaps are deployed, flow divergence behind the nacelle increases significantly, which follows expectation as the flap increases wing circulation, resulting in a steeper spanwise pressure gradient from the wing centerline. Figure 13 shows OFV of the wing with deployed flap at $\alpha = 10$ degrees. Again, the thick dashed line approximates the separation line across the wing. In both cases, flow separation induced by the nacelle increases significantly compared to the flap nested configuration at the same angle of attack. The divergent flow region behind the nacelle spans a much wider portion of the wing and the boundary layer accumulation becomes visible as diffuse regions (I) in the oil flow. The wing leading edge at the nacelle-wing junction shows reversed flow (II) ahead of the zigzag tape and vortex structures (III) can be observed in the nacelle-wing junction where flow coming off of the nacelle circulates into the reversed flow region. Downstream of the zigzag tape the flow seems to be attached and diverging (IV) due to the high pressure region in the nacelle. This is indicative of a leading edge separation bubble in the nacelle-wing junction as described by Qiu et al. [24] and also noted in the recent dissertation by van Arnhem [26].

Based on the OFV, the flap flow seems to have little interference from the nacelle effects. The 15 degrees flap case shows no interaction besides separation induced on the outer part of the flap due to interference with the flap brackets (VI). A slight induction of trailing edge separation can be observed downstream of the nacelle (V), which is likely related to the lack of pressure recovery region in the wake of the main element, inducing slight trailing edge separation on the flap. A similar structure is observed on the 30 degrees flap. Note also the major effect of the flap brackets on the flow on the 30 degrees flap, which induces early separation and removes the laminar separation bubble, marked by the dash-dotted line (VII).

Local pressure distributions (Fig. 14) confirm that the loading of the 15 degrees flap is hardly affected by the nacelle interference on the main element, but the 30 degrees case shows a loss of suction on the flap at $\alpha = 10°$. This is likely caused by the separated wake of the main element induced by the nacelle effects, which significantly alters the off-the-surface flow characteristics above the flap.

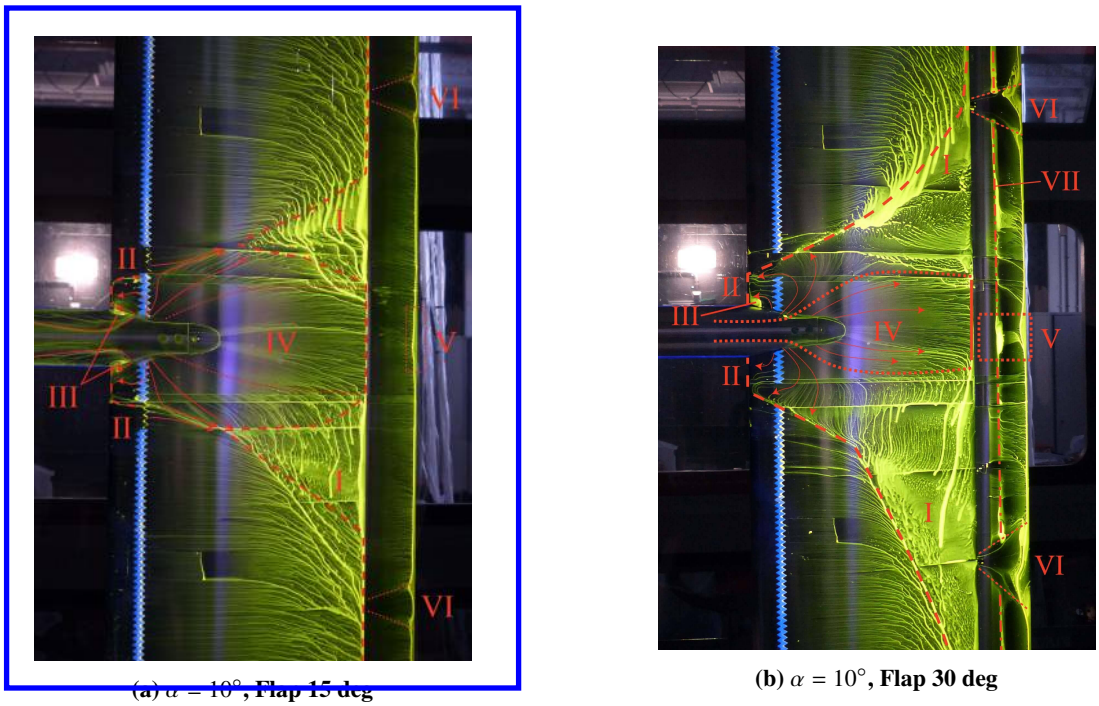

(a) $\alpha = 10^{\circ}$**, Flap 15 deg** **(b)** $\alpha = 10^{\circ}$**, Flap 30 deg**

Fig. 13 Oil flow visualization images of the wing with nacelle mounted at different flap settings, showing the development of the flow expansion behind the nacelle with increasing flap deflection. Dashed line indicates the approximate separation line, dash-dotted line shows a laminar separation bubble.

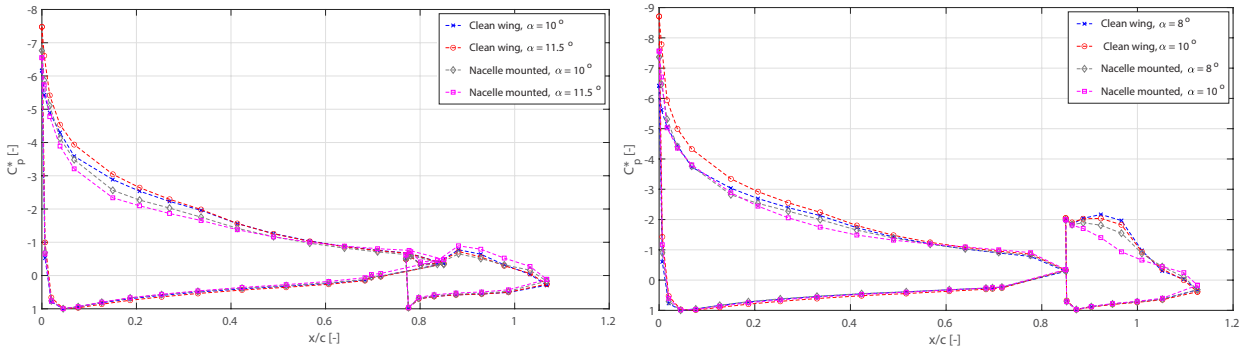

(a) Flap 15 deg **(b) Flap 30 deg**

Fig. 14 Comparisons of pressure distributions on the port side for clean wing and nacelle mounted (unpowered) configurations for the two flap deflections around the angle of maximum lift coefficient for the nacelle mounted cases.

C. Slipstream Interference

Propeller-wing interaction phenomena are well documented in literature, for instance in the work of Veldhuis [14]. It is a highly coupled system, which is inherently captured in experiments and cannot be separated. However, only measurements regarding the wing performance were taken during the experiment and thus this paper will discuss only the interference effects of the slipstream on the wing aerodynamics, despite this being a result of the 2-way (or in case of flap deployment 6-way) interaction between propeller-wing(-flap).

1. Sectional Aerodynamic Coefficients

The basic effects of the slipstream on wing performance can be captured by viewing the slipstream as an increase in dynamic pressure, increasing lift generation, and a tangential velocity that induces a local change in angle of attack [14]. These effects are immediately obvious from the sectional aerodynamic coefficients presented in Fig. 15 through 17, respectively showing the local integrated aerodynamic coefficients for flaps at 0, 15 and 30 degrees at various advance ratios (unpowered, $J = 1.0$ and $J = 0.8$). Note that the unpowered configurations have the nacelle mounted, as it has a large effect on the local flow behavior and therefore offers a better reference for assessment of the slipstream interactions.

Regardless of the flap setting, the maximum lift is increased for the powered configuration compared to the unpowered configurations with nacelle. The tangential velocity in the slipstream changes the local effective angle of attack at the wing, causing asymmetry in the local lift, drag and moment coefficients between port and starboard side measurement locations. As angle of attack increases the offset between the lift coefficient of the port and starboard sides decreases. This may be attributed to the swirl recovery effect which becomes stronger with increasing wing circulation [14], or to asymmetric disk loading due to the angle of attack. The angle at which maximum lift is achieved changes only 0.5-1 degrees for each of the powered configurations compared to the unpowered configurations, even for the down-going blade side where effective angle of attack on the wing is reduced due to the tangential velocity in the slipstream. This is at least in part due to the nacelle inclination of 5 degrees compared to the wing chord, which will counteract the effective decrease in angle of attack on the down-going blade side where otherwise a higher relative angle of maximum lift would be expected.

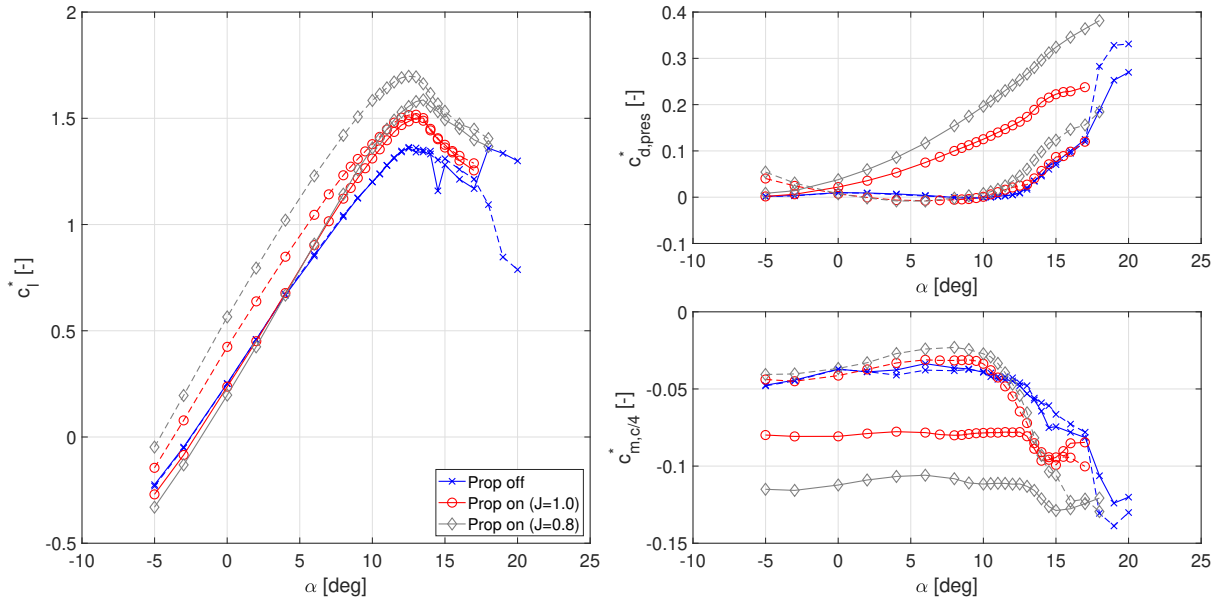

Fig. 15 Integrated local pressure measurements versus angle of attack for wing with flap nested in unpowered (nacelle mounted) and propeller on configurations. Solid and dashed lines represent respectively down- and up-going blade sides. Uncorrected wind tunnel data.

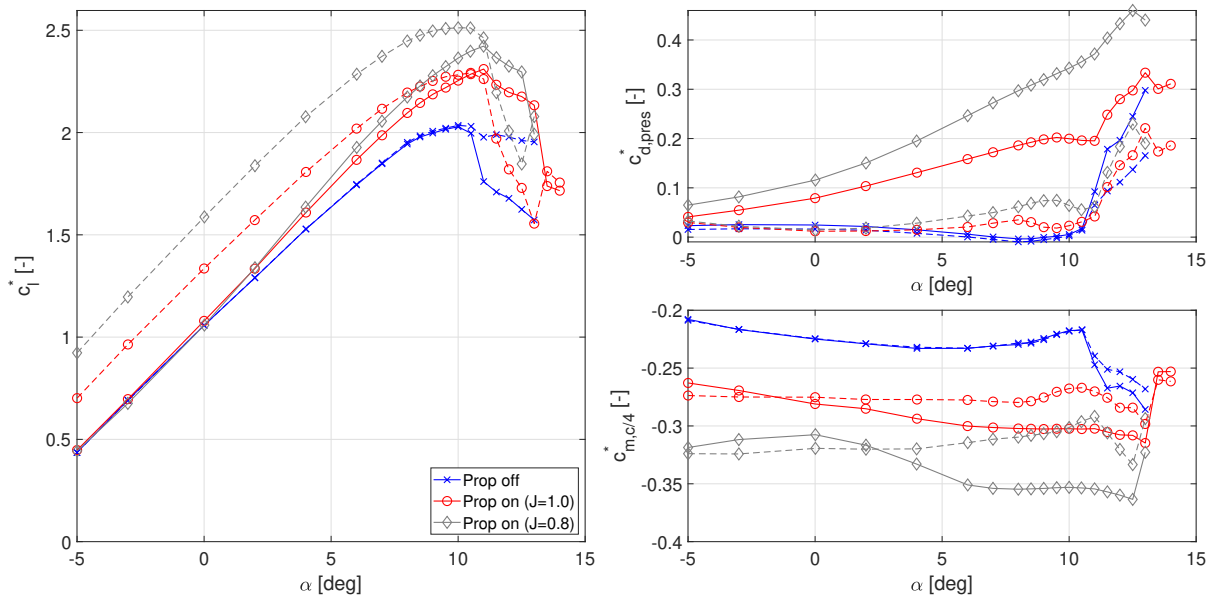

Fig. 16 Integrated local pressure measurements versus angle of attack for wing with flap deployed ($d_f = 15°$, $dx = 8\%$, $ds = 8\%$) in unpowered (nacelle mounted) and propeller on configurations. Solid and dashed lines represent respectively down- and up-going blade sides. Uncorrected wind tunnel data.

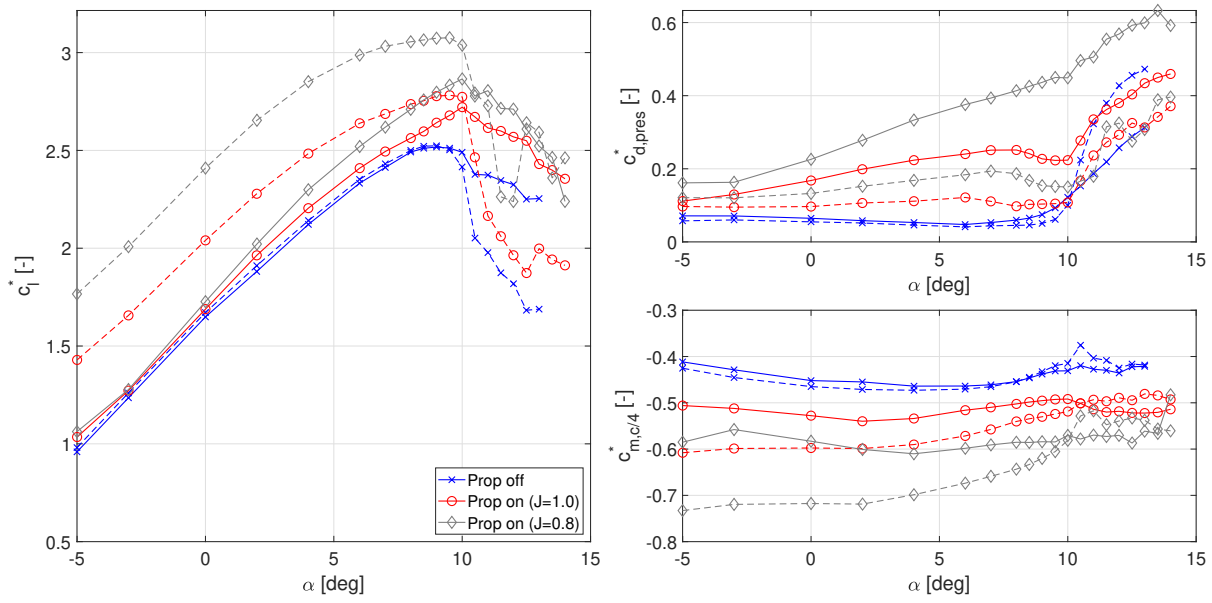

Fig. 17 Integrated local pressure measurements versus angle of attack for wing with flap deployed ($d_f = 30°$, $dx = 0\%$, $ds = 3\%$) in unpowered (nacelle mounted) and propeller on configurations. Solid and dashed lines represent respectively down- and up-going blade sides. Uncorrected wind tunnel data.

2. Propeller-Wing Interactions

Oil flow visualizations of the wing in powered conditions gives more insight into the overall aerodynamic phenomena that occur on the wing in the powered cases. Figure 18 shows the OFV of the powered flap nested case (CF10) at $J = 0.8$ for three angles of attack. It clearly shows the area affected by the propeller slipstream, the edge of which moves spanwise towards the down-going blade side as it passes the wing (I). The down-going blade side shows most deformation in the first 20% of the chord, while the up-going blade side shows most deformation towards the rear 50% chord. The latter seems to decrease as angle of attack increases, though it is impossible to verify only based on the OFV. Within the slipstream boundaries, the flow expands as it moves over the wing (II), opposite to the main swirl direction. This expansion increases with increasing angle of attack. On the nacelle, a flow in opposite direction to the main swirl component can also be observed (III). It is likely that this is a result of the root vortex system, which moves over the wing slightly above the surface. This reveals a pitfall of OFV for slipstream interaction, as the off-the-surface flow characteristics may be dominant for the wing performance but cannot be visualized.

As angle of attack increases, areas of separated flow start to form on the outside of the slipstream affected area. These are believed to be caused by local increases in angle of attack induced by vorticity shed into the wake due to the disturbance of the spanwise lift distribution caused by the slipstream [14]. At $\alpha = 13$ degrees, the separated areas displace the boundaries of the slipstream (at least on-the-surface) causing a significant reduction in affected area of the wing. At $\alpha = 0$ degrees, some interference can be observed on the separation line at the trailing edge (V), which seems to originate from the nacelle and induces slight trailing edge separation. This area moves spanwise as the expansion of on-the-surface flow within the streamline increases with angle of attack. At $\alpha = 13$ degrees, this area of separated flow seems to have merged with the larger separated area on the outside boundary of the slipstream. Preliminary numerical simulations show that this area is in fact two regions of flow that originate from each nacelle-wing junction. It is hypothesized that this may be the root vortex system coming off of the nacelle and interacting with the wing, but further investigation is required to confirm this.

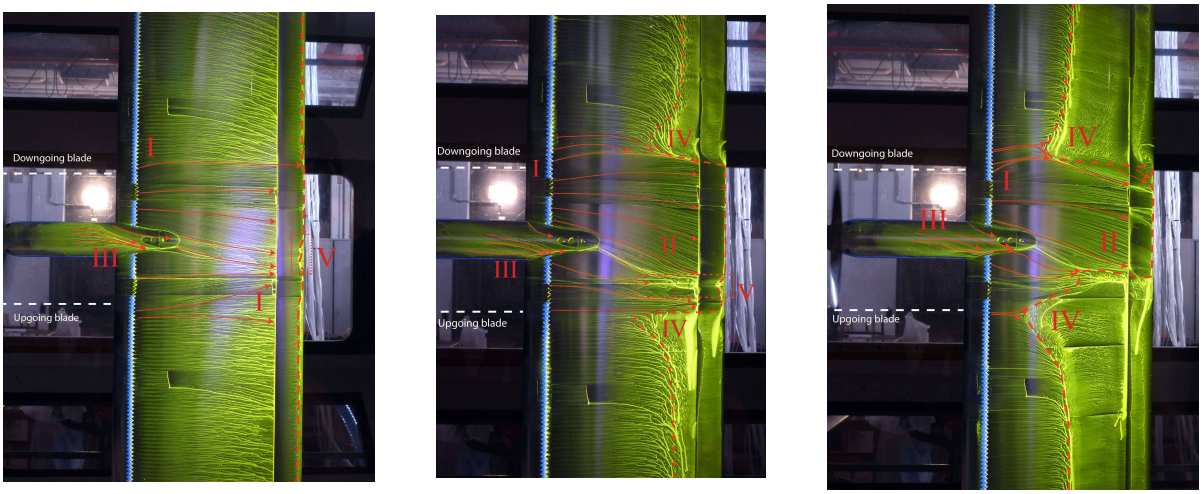

(a) $\alpha = 0°$ **(b)** $\alpha = 10°$ **(c)** $\alpha = 13°$

Fig. 18 Oil flow visualization images of the wing with flap nested and nacelle installed (CF9), showing attached flow directly behind the nacelle and early onset of separation originating from the nacelle-wing junction.

Overall, the OFV illustrates the complexity of the propeller-wing interactive flowfield. Local deformation of streamlines within the slipstream are highly variable and slipstream deformation shows to be highly dependent on spanwise loading. Furthermore, the importance of volumetric / off-the-surface flow visualization is underlined, as on-the-surface flows seem to move in opposite direction to the swirl in the main body of the slipstream. Finally, the importance of spanwise resolution is exemplified, as the flow is highly three-dimensional. Although the pressure taps on the downgoing blade side (identifiable by the taped off region on either side of the nacelle) seems to be positioned in a streamwise-oriented part of the slipstream, the port-side pressure taps see crossflow components, making any interpretation of the measurements as a two-dimensional wing section impossible.

3. Propeller-Wing-Flap Interactions

Figure 19 shows the OFV of both the pressure and suction side of the powered case with 30 degrees flap at $J = 0.8$ and $\alpha = 8$ degrees. On the main element, most of the same structures as described for the flap nested cases in section III.C.2 can be seen. The flap flow shows some interesting differences, however. The slipstream affected area can be determined by the disappearance of the laminar separation bubble, due to early transitioning of the boundary layer in the slipstream [27]. The area of the flap affected by the slipstream (VII) can be seen to be much wider than and offset from the slipstream-affected area on the main element. At the edge and roughly in the middle of this area, several vortical structures are observed (V), likely due to root and tip vortex interactions. Figure 19b shows that the offset from the main element is because the flap is immersed in the flow coming off of the pressure side of the main element, which undergoes significant deformation before it reaches the flap. For different spanwise stations the flow around the flap thus varies, impacting performance. This impact can be recognized from the shift in separation line on the flap within the slipstream-affected area.

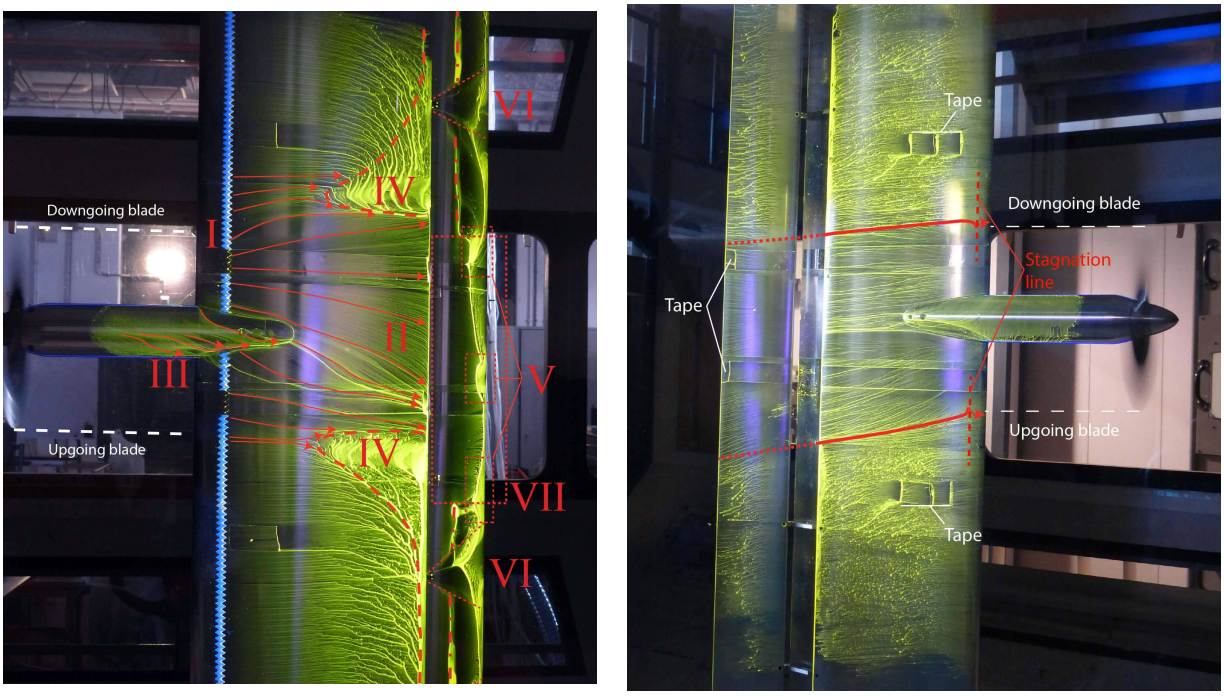

(a) Suction side

(b) Pressure side

Fig. 19 Oil flow visualization of both sides of the wing for the powered configuration with flap deployed at 30 degrees (CF6), $J = 0.8$, $\alpha = 8$ degrees, showing the deformation of the slipstream and impingement of the pressure side slipstream half on the flap.

The images of Fig. 19 show that the flow seen by the flap (and therefore its performance) is highly dependent on the interaction of the slipstream with the main element (and therefore the interaction with the flap). Simplified numerical analyses such as streamtube models will thus quickly break down when representing propeller-wing-flap systems, as they will not accurately represent the area of the flap being immersed in the slipstream, nor the concentrations of dynamic pressure that will result from the slipstream deformation over the main element. Furthermore, this insight is of importance to distributed propulsion application of propeller-blown lift augmentation, as it shows that slipstreams of closely spaced propellers will have to interact. Some notion of this can already be found in recent advanced numerical simulations of distributed propulsion flows, such as Keller [28].

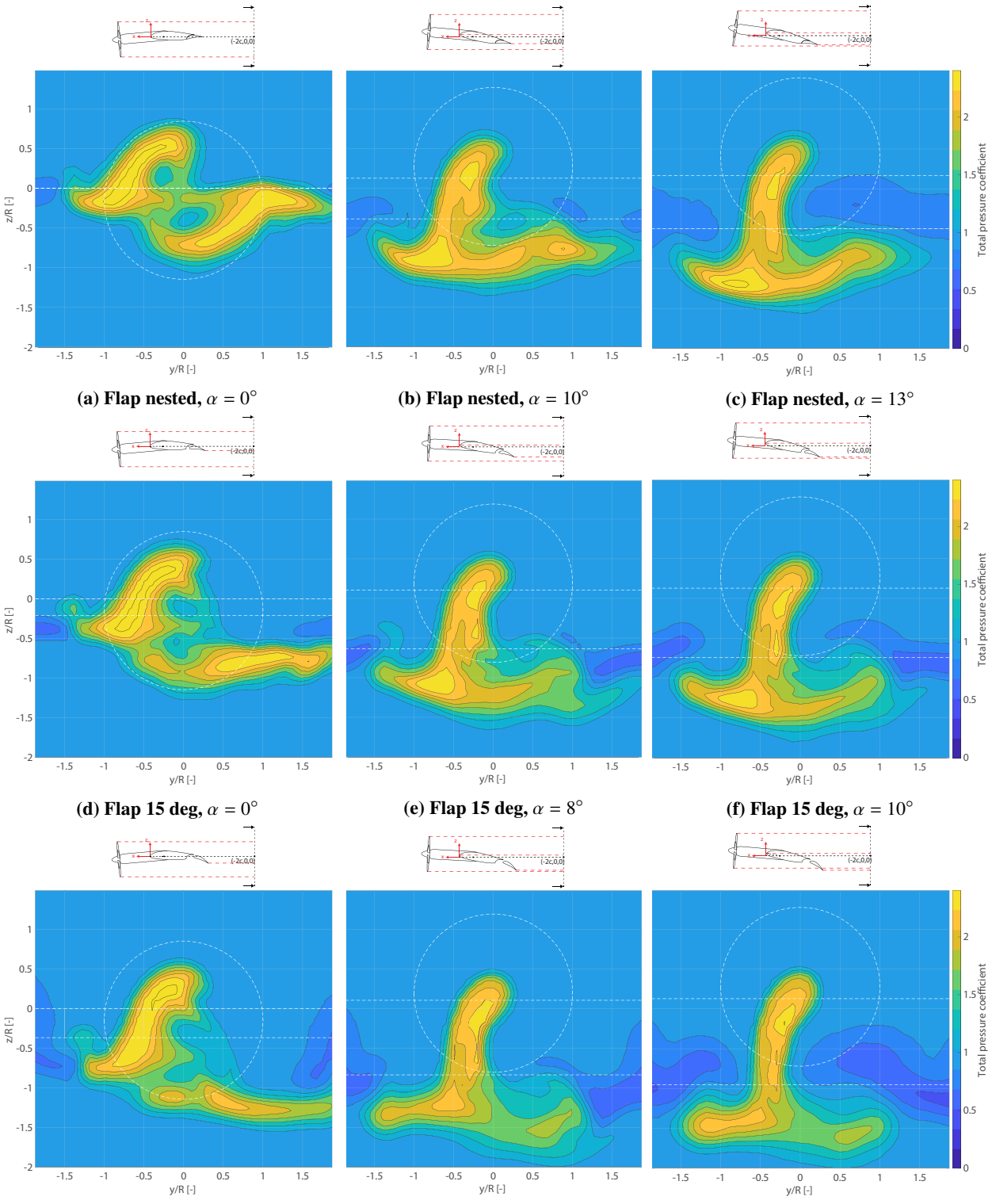

(a) Flap nested, $\alpha = 0°$ **(b) Flap nested, $\alpha = 10°$** **(c) Flap nested, $\alpha = 13°$**

(d) Flap 15 deg, $\alpha = 0°$ **(e) Flap 15 deg, $\alpha = 8°$** **(f) Flap 15 deg, $\alpha = 10°$**

(g) Flap 30 deg, $\alpha = 0°$ **(h) Flap 30 deg, $\alpha = 8°$** **(i) Flap 30 deg, $\alpha = 10°$**

Fig. 20 Total pressure in the yz-plane at $x/c = -2$ for various powered configurations at $J = 0.8$. View in streamwise direction. Dashed lines indicate projections of the propeller, leading- and trailing edge on the yz-plane. Pressure taps are located at $y/R = \pm 0.7$

D. Downstream Slipstream Deformation

To shed further light on the slipstream deformation and its interaction with a flap, total pressure measurements in the wake were analyzed. Figure 20 shows the total pressure coefficient, defined by equation (1), in the zy-plane at $x/c = -2$ (meaning one chord behind the trailing edge of the airfoil with flap nested at $\alpha = 0$ degrees). Since the propeller adds total pressure to the flow, the slipstream can be identified as areas where the total pressure coefficient is larger than unity. Note that due to the interaction with the deficit in total pressure caused by the viscous wake of the wing, the edges of the slipstream become difficult to define exactly in the presence of significant separation.

$$C_{p,tot} = \frac{P_{rake} - P_\infty}{q_\infty} \tag{1}$$

For the flap nested configuration at $\alpha = 0$ degrees, the slipstream undergoes the typical anti-symmetrical shear. As angle of attack increases, the slipstream deforms into an inverted T-shape. For $\alpha = 0$ degrees, the root vortex system and nacelle wake can be clearly identified as a reduction in total pressure in each half of the slipstream. At higher angles of attack, this system is displaced towards the upper-right quadrant as the two halves merge. As a result of the vorticity shed from the wing due to the enhanced lift within the slipstream, the upper half of the slipstream is compressed towards the middle, while the lower half of the slipstream is elongated in spanwise direction. The OFV images in section III.C.3 show that at least a part of this elongation already occurs on the wing surface, while the compression of the upper half of the slipstream cannot be observed.

As the flap is deployed, the anti-symmetrical shear is no longer the dominant deformation effect at $\alpha = 0$ degrees. Rather, the bottom half of the slipstream is displaced and elongated significantly. The upper half of the slipstream is much less affected, mainly showing a vertical displacement due to additional circulation on the wing. As angle of attack increases, the slipstream attains a similar inverted-T shape as with flap nested. Local concentrations of total pressure towards positive y/D seem to decrease with increased flap deflection. The seemingly limited extent of the slipstream into the positive y/D direction for high angles of attack and flaps deployed is believed to be due to the interaction with the wing wake, as the low angle of attack results show the slipstream to extend to well beyond $y/D = 0.8$ for 30 degrees flap.

IV. Conclusion

Wind tunnel experiments were performed on a straight, untapered wing with single slotted flap and single propeller in order to investigate the interactive flows occurring in propeller-wing-flap systems. Results were captured for three flap settings, being flap nested, flap deployed at 15 degrees and flap deployed at 30 degrees, with a clean wing, wing with nacelle mounted (unpowered) and wing with powered propeller.

Discrepancies between the obtained results and reference data were mainly attributed to the difference in Reynolds number, the forced boundary layer transition with zigzag tape and local nature of the pressure measurements. Particularly the latter were shown to be affected by three-dimensional flow structures common to quasi-2D wind tunnel setups with high aspect ratios, complicating data interpretation. Combined with the three-dimensional flow characteristics due to the nacelle-wing and propeller-wing(-flap) interactions, the need for higher spanwise resolution of pressure measurements when achieving validation datasets is illustrated. Similarly, the limitation of on-the-surface only measurements are exposed for propeller-wing(-flap) validation experiments, thus stressing the necessity of volumetric flow quantification using e.g. PIV.

Using oil flow visualization, the main nacelle-wing interactions were shown. The nacelle induced large areas of separation on the wing due to boundary layer accumulation originating from the nacelle-wing junction. The spanwise extent of this separation is dependent on the spanwise pressure gradient between the flow behind the nacelle and the flow outboard of the nacelle, thus increasing in size with increased flap deflection. With flaps deflected and high angles of attack, evidence of separation bubbles in the nacelle-wing junction was found, which agreed well with literature.

Powered cases showed common propeller-wing interference effects that are expected from literature, such as the increased lift due to additional dynamic pressure in the slipstream and the induced angles of attack due to swirl. Oil flow visualization showed the slipstream to expand on the suction side in opposite direction to the swirl, illustrating the pitfalls of on-the-surface flow analysis for slipstream interactions. The powered cases with deployed flaps showed the same main phenomena on the main element as the flap nested cases, however the flap was shown to be immersed for a

wider portion of its span and at a location offset from the main element. This was traced to the flap being immersed in the lower half of the slipstream that passes the pressure side of the main element, which significantly deforms before reaching the flap. Further research on the subject of slipstream deformation for propeller-wing-flap systems is needed to fully understand the system interactions.

Analysis of the slipstream deformation in a plane one chord downstream of the wing showed that deploying the flap alone has a significant effect on the deformation of the lower half of the slipstream, but does not affect the upper half as much. When increasing angle of attack, all cases showed the typical inverted-T shape of the slipstream. Due to the significant viscous wing wakes in the flapped cases, the actual effect of flap deflection on downstream slipstream deformation at high angles of attack was difficult to judge and further investigation would be required.

Appendix

A. Pressure tap locations

Table 2 Locations of pressure taps on main element.

port no.		x/c	y/c
1	46	0.7767	0.0492
2	47	0.7100	0.0605
3	48	0.6400	0.0716
4	49	0.5667	0.0824
5	50	0.4900	0.0925
6	51	0.4133	0.1007
7	52	0.3367	0.1050
8	53	0.2700	0.1035
9	54	0.2067	0.0977
10	55	0.1500	0.0879
11	56	0.1067	0.0764
12	57	0.0683	0.0620
13	58	0.0383	0.0458
14	59	0.0167	0.0291
15	60	0.0050	0.0148
16	61	0.0000	0.0000
17	62	0.0067	-0.0113
18	63	0.0200	-0.0196
19	64	0.0450	-0.0279
20	65	0.0767	-0.0349
21	66	0.1267	-0.0427
22	67	0.1867	-0.0497
23	68	0.2533	-0.0553
24	69	0.3300	-0.0601
25	70	0.4233	-0.0632
26	71	0.5167	-0.0632
27	72	0.6067	-0.0594
28	73	0.6833	-0.0494
29	74	0.6970	-0.0300
30	75	0.7167	0.0044
31	76	0.7467	0.0253

Table 3 Locations of pressure taps on flap (in nested position).

port no.		x/c	y/c
32	77	0.9600	0.0125
33	78	0.9000	0.0260
34	79	0.8467	0.0334
35	80	0.7983	0.0316
36	81	0.7550	0.0205
37	82	0.7233	0.0017
38	83	0.7067	-0.0160
39	84	0.7000	-0.0311
40	85	0.7083	-0.0416
41	86	0.7300	-0.0386
42	87	0.7617	-0.0309
43	88	0.8067	-0.0202
44	89	0.8600	-0.0094
45	90	0.9167	-0.0019

Acknowledgments

The authors would like to acknowledge Dr. ir. R. de Vries for his significant contribution with the test setup and troubleshooting during the experimental campaign. Furthermore, the authors would like to acknowledge the partial

funding by the Deutsche Forschungsgemeinschaft (DFG, German Research Foundation) under Germany's Excellence Strategy - EXC 2163/1 - Sustainable and Energy Efficient Aviation - Project-ID 390881007.

References

[1] Kuhn, R. E., and Draper, J. W., "An Investigation of a Wing-Propeller Configuration Employing Large-Chord Plain Flaps and Large-Diameter Propellers for Low-Speed Flight and Vertical Take-Off," NACA Technical Note 3307, National Advisory Committee for Aeronautics, 1954.

[2] Kuhn, R. E., "Investigation of the effects of ground proximity and propeller position on the effectiveness of a wing with large-chord slotted flaps in redirecting propeller slipstreams downward for vertical take-off," NACA Technical Note 3629, National Advisory Committee for Aeronautics, 1956.

[3] Kuhn, R. E., "Semiempirical Procedure for Estimating Lift and Drag Characteristics of Propeller-Wing-Flap Configurations for Vertical- and Short-Take-Off-And-Landing Airplanes," NASA Memorandum 1-16-59L, National Aeronautics and Space Administration, 1959. URL `http://ntrs.nasa.gov/archive/nasa/casi.ntrs.nasa.gov/19980232082.pdf`.

[4] Viken, J. K., Viken, S., Deere, K. A., and Carter, M., "Design of the Cruise and Flap Airfoil for the X-57 Maxwell Distributed Electric Propulsion Aircraft," *35th AIAA Applied Aerodynamics Conference*, American Institute of Aeronautics and Astronautics, Reston, Virginia, 2017, pp. 1–41. https://doi.org/10.2514/6.2017-3922, URL https://arc.aiaa.org/doi/10.2514/6.2017-3922.

[5] Stoll, A. M., Bevirt, J., Moore, M. D., Fredericks, W. J., and Borer, N. K., "Drag Reduction Through Distributed Electric Propulsion," *14th AIAA Aviation Technology, Integration, and Operations Conference*, American Institute of Aeronautics and Astronautics, Reston, Virginia, 2014, pp. 16–20. https://doi.org/10.2514/6.2014-2851, URL https://arc.aiaa.org/doi/10.2514/6.2014-2851.

[6] Deere, K. A., Viken, S. A., Carter, M. B., Viken, J. K., Wiese, M. R., and Farr, N., "Computational analysis of powered lift augmentation for the LEAPTech distributed electric propulsion wing," *35th AIAA Applied Aerodynamics Conference, 2017*, 2017, pp. 1–20. https://doi.org/10.2514/6.2017-3921.

[7] Agrawal, D. R., Asad, F., Berk, B., Long, T., Lubin, J., Courtin, C., Drela, M., Hansman, R. J., and Thomas, J., "Wind Tunnel Testing of a Blown Flap Wing," *AIAA Aviation Forum*, American Institute of Aeronautics and Astronautics, Dallas, Texas, 2019, pp. 1–20. https://doi.org/10.2514/6.2019-3170.

[8] Courtin, C., Hansman, R. J., and Drela, M., "Flight Test Results of a Subscale Super-STOL Aircraft," *AIAA SciTech Forum*, American Institute of Aeronautics and Astronautics, Orlando, Florida, 2020, pp. 1–15. https://doi.org/10.2514/6.2020-0977.

[9] Fei, X., German, B. J., and Patterson, M. D., "Exploring the effects of installation geometry in high-lift propeller systems," *AIAA SciTech Forum*, American Institute of Aeronautics and Astronautics, Kissimmee, Florida, 2018, pp. 1–24. https://doi.org/10.2514/6.2018-0277.

[10] Bohari, B., Borlon, Q., Mendoza-Santos, P. B., Sgueglia, A., Benard, E., Bronz, M., and Defoort, S., "Conceptual Design of Distributed Propellers Aircraft: Non-Linear Aerodynamic Model Verification of Propeller-Wing Interaction in High-Lifting Configuration," *2018 AIAA Aerospace Sciences Meeting*, American Institute of Aeronautics and Astronautics, Reston, Virginia, 2018, pp. 1–27. https://doi.org/10.2514/6.2018-1742, URL https://arc.aiaa.org/doi/10.2514/6.2018-1742.

[11] Beck, N., Radespiel, R., Lenfers, C., Friedrichs, J., and Rezaeian, A., "Aerodynamic effects of propeller slipstream on a wing with circulation control," *Journal of Aircraft*, Vol. 52, No. 5, 2015, pp. 1422–1436. https://doi.org/10.2514/1.C032901.

[12] Kroo, I., "Propeller-Wing Integration for Minimum Induced Loss." *Journal of Aircraft*, Vol. 23, No. 7, 1986, pp. 561–565. https://doi.org/10.2514/3.45344.

[13] Witkowski, D. P., Johnston, R. T., and Sullivan, J., "Propeller/Wing Interaction," *27th Aerospace Sciences Meeting*, American Institute of Aeronautics and Astronautics, Reno, Nevada, 1989, pp. 1–13.

[14] Veldhuis, L., "Propeller wing aerodynamic interference," Phd dissertation, Delft University of Technology, 2005. URL http://www.narcis.nl/publication/RecordID/oai:tudelft.nl:uuid:8ffbde9c-b483-40de-90e0-97095202fbe3.

[15] Roosenboom, E. W., Stürmer, A., and Schröder, A., "Advanced experimental and numerical validation and analysis of propeller slipstream flows," *Journal of Aircraft*, Vol. 47, No. 1, 2010, pp. 284–291. https://doi.org/10.2514/1.45961.

[16] Schroijen, M. J., Veldhuis, L. L., and Slingerland, R., "Propeller slipstream investigation using the fokker F27 wind tunnel model with flaps deflected," *ICAS Secretariat - 26th Congress of International Council of the Aeronautical Sciences 2008, ICAS 2008*, Vol. 3, 2008, pp. 2181–2194.

[17] Boermans, L., and Rutten, P., "Two-dimensional aerodynamic characteristics of airfoil NLF-MOD22 with fowler flap," Tech. rep., Delft University of Technology, Delft, 1995.

[18] Allen, H. J., and Vincenti, W. G., "Wall interference in a two-dimensional-flow wind tunnel, with consideration of the effect of compressibility," NACA Technical Report 782, National Advisory Committee of Aeronautics, 1944.

[19] Barlow, J. B., Rae, W. H., and Pope, A., *Low-Speed Wind Tunnel Testing*, 3rd ed., John Wiley & Sons, Inc., 1999.

[20] Braslow, A. L., and Knox, E. C., "Simplified Method for Determination of Critical Height of Distributed Roughness Particles for Boundary-Layer Transition at Mach Numbers from 0 to 5," NACA Technical Note 4363, National Advisory Committee for Aeronautics, Langley Field, Va., 1958.

[21] Yon, S. A., and Katz, J., "Study of the unsteady flow features on a stalled wing," *AIAA Journal*, Vol. 36, No. 3, 1998, pp. 305–312. https://doi.org/10.2514/2.372.

[22] Broeren, A. P., and Bragg, M. B., "Spanwise variation in the unsteady stalling flowfields of two-dimensional airfoil models," *AIAA Journal*, Vol. 39, No. 9, 2001, pp. 1641–1651. https://doi.org/10.2514/2.1501.

[23] Winkelmann, A. E., and Barlow, J. B., "Flowfield model for a rectangular planform wing beyond stall," *AIAA Journal*, Vol. 18, No. 8, 1980, pp. 1006–1008. https://doi.org/10.2514/3.50846.

[24] Qiu, Y., Bai, J., and Qiao, L., "Aerodynamic Effects of Wing-Mounted Engine Nacelle on High-Lift Configuration of Turboprop Airliner," *Journal of Aircraft*, Vol. 55, No. 3, 2018, pp. 1082–1089. https://doi.org/10.2514/1.C034529, URL https://arc.aiaa.org/doi/10.2514/1.C034529.

[25] Radespiel, R., Heinze, W., and Bertsch, L., "High-Lift Research for Future Transport Aircraft," *66. Deutscher Luft- and Raumfahrtkongress (DLRK)*, 2017, pp. 1–15.

[26] van Arnhem, N., "Unconventional Propeller-Airframe Integration for Transport Aircraft Configurations," Phd dissertation, Delft University of Technology, 2022. https://doi.org/10.4233/uuid:4d47b0db-1e6a-4f38-af95-aafd33c29402Publication.

[27] Miley, S. J., Howard, R. M., and Holmes, B. J., "Wing laminar boundary layer in the presence of a propeller slipstream," *Journal of Aircraft*, Vol. 25, No. 7, 1988, pp. 606–611. https://doi.org/10.2514/3.45630.

[28] Keller, D., "Towards higher aerodynamic efficiency of propeller-driven aircraft with distributed propulsion," *CEAS Aeronautical Journal*, Vol. 12, No. 4, 2021, pp. 777–791. https://doi.org/10.1007/s13272-021-00535-5, URL https://doi.org/10.1007/s13272-021-00535-5https://link.springer.com/10.1007/s13272-021-00535-5.